Journal of Solid State Electrochemistry (2023) 27:705–714
https://doi.org/10.1007/s10008-022-05363-z

ORIGINAL PAPER

The role of scavengers in the CdS film corrosion

Cristian Hessel[1] · **Nickson Perini**[1] · **Elton Sitta**[1]

Received: 14 October 2022 / Revised: 9 December 2022 / Accepted: 19 December 2022 / Published online: 28 December 2022

Abstract

The cadmium sulfide (CdS) is one of the most applied chalcogenides to the water splitting (WS) on photoelectrochemical cells (PEC). The CdS bandgap is 2.4 eV which suits very well with the solar spectrum. Unfortunately, because to the high overpotential and sluggish kinetic of the oxygen evolution reaction (OER) on the anodic compartment of the PEC, the pristine form of CdS film undergoes photocorrosion. In this work, using a series of small organic molecules as alternatives for the OER on the CdS/FTO photoanodes under visible light irradiation in Na_2SO_4 0.5 mol L^{-1} solution, we explored the dependence of the CdS photocorrosion and the oxidation reaction of small organic molecules. Comparing the methanol, ethylene glycol, and glycerol oxidation reactions, the glycerol showed higher photocurrents in both linear potential voltammetry and chronopotentiostatic experiments. We also employed cross-sectional SEM images to investigate pristine and aged CdS films revealing distinct photocorrosion patterns depending on organic molecule employed. The results suggest the CdS film degradation relates to the low ability of water in scavenge the photogenerated holes and the presence of high reactive species, such as glycerol, capture these holes decreasing the CdS corrosion.

Keywords CdS · Photocorrosion · Photoelectrocatalysis · Glycerol oxidation · Ethylene glycol oxidation · Methanol oxidation

Introduction

The cadmium sulfide (CdS) is an active visible-light sensitive photocatalyst material with 2.4 eV bandgap that is suitable to application under visible light irradiation [1]. It is well known that light absorption with energy higher than bandgap leads to the formation of electrons (e^-) and holes (h^+) [2, 3] in aqueous solutions. While photogenerated electrons reduce protons, yielding H_2, holes capture electrons from species in the electrolyte, for instance, water, organic and inorganic compounds, and even the elements from the photoanode, e.g., sulfur from CdS film structure [4], explaining the photocorrosion process by the irreversible hole-driven oxidation of the photoanode surface [5]. Specifically, CdS undergoes photocorrosion in presence of oxygen as follows (Eq. 1 and Eq. 2) [6, 7]:

$$CdS \xrightarrow{h\nu} e^-_{CB}(CdS) + h^+_{VB}(CdS) \quad (1)$$

$$CdS + 4h^+ + 2H_2O + O_2 \rightarrow Cd^{2+} + SO_4^{2-} + 4H^+ \quad (2)$$

In the absence of oxygen, the photocorrosion also takes place, but it is caused by two photogenerated holes yielding sulfur (Eq. 3) [6], conversely, CdS is partially dissolved due to the chemical equilibrium with Cd^{2+} and S^{2-} (Eq. 4) and their secondary dependences with solution pH (Eqs. 5 and 6).

$$CdS + 2h^+ \rightarrow Cd^{2+} + S \quad (3)$$

$$CdS \rightleftharpoons Cd^{2+} + S2^{2-} \quad (4)$$

$$Cd^{2+} + 2OH^- \rightleftharpoons Cd(OH)_2 \quad (5)$$

$$S^{2-} + 2H^+ \rightleftharpoons H_2S \quad (6)$$

Several strategies to inhibit photocorrosion have been described on the literature, including the use of protective layers [8, 9], heterojunctions [10, 11], or adding a sacrificial agent to the solution to capture the photogenerated holes of the valence band of the semiconductor [12–14]. The sacrificial agents scavenge the holes of the valence band easier than

✉ Elton Sitta
esitta@ufscar.br

[1] Federal University of Sao Carlos, 13565-905 Sao Carlos-SP, Brazil

sulfur anions from CdS film, because its oxidation potential is lower than that for sulfur oxidation [15]. Oxygen evolution reaction (OER) can provide electrons to the holes; however, the standard potential for the OER is relatively high (1.23 V vs SHE) and the four-electron transfer to produce O_2 has kinetic limitations. Furthermore, the oxygen evolution induces the photocorrosion as described by Eq. (2).

Other hole scavengers such as hydrogen peroxide, sulfite, and oxalic acid are largely employed to measure the maximum activity of material i.e., the maximum amount of hole generated in the valence band without kinetic limitations. Interestingly, more than provide an activity limit value, the oxidation of organic molecules may produce high-added value products, which is very attractive from an economic point of view [16], once while the cathode is devoted to produce H_2, the products of anode reaction can be employed on the industry.

Methanol [17–19], ethanol [20], and oxalic acid [21, 22] are examples of small organic molecules that have been applied in photoelectrochemical cell (PEC) anodes to increase the hole scavenge coupled to the production of added-value products or even CO_2. Glycerol, one of the main biodiesel by-products, is also an important and abundant biomass-related compound [23] with the possibility to yield commercially valuable oxidation products as dihydroxyacetone, glyceraldehyde, and glyceric acid [24]. Therefore, glycerol oxidation seems to be a good substitute for OER on the photoanode compartment of the PEC improving the system overall efficiency. In this work, we compare the use of water, methanol, ethylene glycol, and glycerol on the anode compartments under visible light illumination composed by CdS thin film deposited onto a fluorine-doped tin oxide (FTO) substrate. The scavengers are compared in terms of photocurrents depicted on both linear potential voltammogram and chronoamperometric curves at 0.6 V vs RHE and photocorrosion inhibition as probed by scanning electron micrography (SEM).

Experimental procedure

Synthesis of CdS photoanode

All chemicals were purchased from Sigma-Aldrich and used without further purification. An Anton Paar Microwave Reactor Monowave 400 was employed to synthesize CdS thin films by the chemical bath deposition. Firstly, the FTO substrate was immersed for 5 min. in a G-30 vial containing 10 mL of a NH_4OH 3.0 mol L^{-1} solution, followed by the addition of 5 mL of a $CdSO_4$ 0.1 mol L^{-1} solution and 5 mL CH_4N_2S 0.15 mol L^{-1} solution. The vial was put into the microwave and heat up to 80 °C for 2 min under constant magnetic stirring. After this, the CdS/FTO was washed in pure water to remove any non-deposited CdS excess and dried in air.

Characterization

XRD measurements were performed using a Shimadzu 6000 diffractometer operating at 30 kV/40 mA, with a copper tube: λkα = 1.5418 Å, in the range of 20–70° (2θ) and a sweep rate of 2° min^{-1}. Raman spectra were obtained using a Witec Raman Microscopy (Ulm, Germany) coupled with a high linear stage and Nikon lens (100X/0.90). Raman signals were excited with a laser Nd: YAG (514 nm; 10 mW). UV–Vis measurements were carried out in a Varian Cary 5E UV–Vis-NIR spectrophotometer, the films were analyzed in the 300–700 nm range. Transmittance mode was employed for this measurement, with a clean FTO substrate as reference. The cross-sectional SEM images were taken in a FEI inspect F50 microscopy. Mott-Schottky plot were obtained by AC techniques with ±10 mV perturbation in three frequencies: 10, 100, and 1000 kHz from 0.2 to 1.2 V vs SHE, with each point being collected at every 50 mV with current stabilization for 15 s.

Photoelectrochemical experiments

A three-electrode electrochemical cell equipped with a quartz window was employed on photoelectrochemical experiments. The system was composed of CdS/FTO (1 × 1 cm^2) as working electrode; a Pt plate (2 × 2 cm^2) as a counter electrode; and a $Ag/AgCl/KCl_{(sat)}$ as reference electrode; however, all the potentials will be expressed in the Reversible Hydrogen Electrode (RHE) scale according to Eq. (7), in which the E_{appl} and $E_{Ag/AgCl/KCl_{(sat)}}$ represent the applied potential and the standard potential for $Ag/AgCl/KCl_{sat}$ electrode (0.197 V vs SHE), respectively.

$$E_{RHE} = E_{appl} + 0.0592pH + E_{Ag/AgCl/KCl_{(sat)}} \quad (7)$$

Na_2SO_4 0.5 mol L^{-1} (pH = 6.5) served as supporting electrolyte with further direct addition of methanol, ethylene glycol, glycerol, or sodium sulfite (Na_2SO_3) in sufficient amounts to yield 0.5 mol L^{-1}. The pH was corrected back to 6.5 after Na_2SO_3 due to the shift caused by the SO_3^{2-}/HSO_3^- equilibrium as discussed on the text. The solar spectrum was simulated with a Newport LCS-100 Class ABB small area solar simulator with 100 mW cm^{-2}. Linear potential voltammetry measurements were taken in the range of 0.0 to 1.0 V vs RHE under dark and simulated solar light regimes at 5 mV s^{-1}. Further light on–off linear potential voltammetry experiments were carried out in the same conditions. Chronoamperometric profiles were also analyzed under and without solar light illumination at a fixed potential (0.6 V vs RHE) for 1 h.

Results and discussion

Characterization

The CdS thin film deposited onto FTO substrates were examined by X-ray diffraction technique (XRD) as shown in Fig. 1a. The peaks highlighted by red circles and black squares correspond to the CdS film and FTO substrate, respectively. The Raman spectra (Fig. 1b) shows two well defined peaks centered at 305 cm^{-1} (1LO) and 605 cm^{-1} (2LO), both related to the longitudinal optical phonons. Figure 1c shows the optical transmittance spectra for the CdS film from 700 to 300 nm (inset) and the $(ahv)^2$ vs $h\nu$ plot, the so-called Tauc plot, in which was estimated the linear behavior at the beginning of adsorption region as indicates by the red solid line. The capacitances (C) of the semiconductor-electrolyte interface for several potentials allowed to build the $1/C^2$ vs E plot, the Mott-Schottky plot (Fig. 1d) and the linear trend observed at low potential was used to obtain the potential value at $1/C^2 = 0$, as shown by the red solid line.

Figure 2 presents the cross-sectional scanning electron microscopy (SEM) image of the synthetized CdS film in pristine form. Clearly, three strictly different regions can be identified: the glass substrate; the ordered crystalline FTO layer with approximately 590 nm; the CdS films with approximately 900 nm thick, showing a globular packed morphology.

Electrochemical measurements and photocorrosion

Figure 3 compares the activity of CdS for water (only supporting electrolyte), glycerol, and sulfite oxidation reactions in the Na_2SO_4 0.5 mol L^{-1} solution with pH = 6.5. The plate

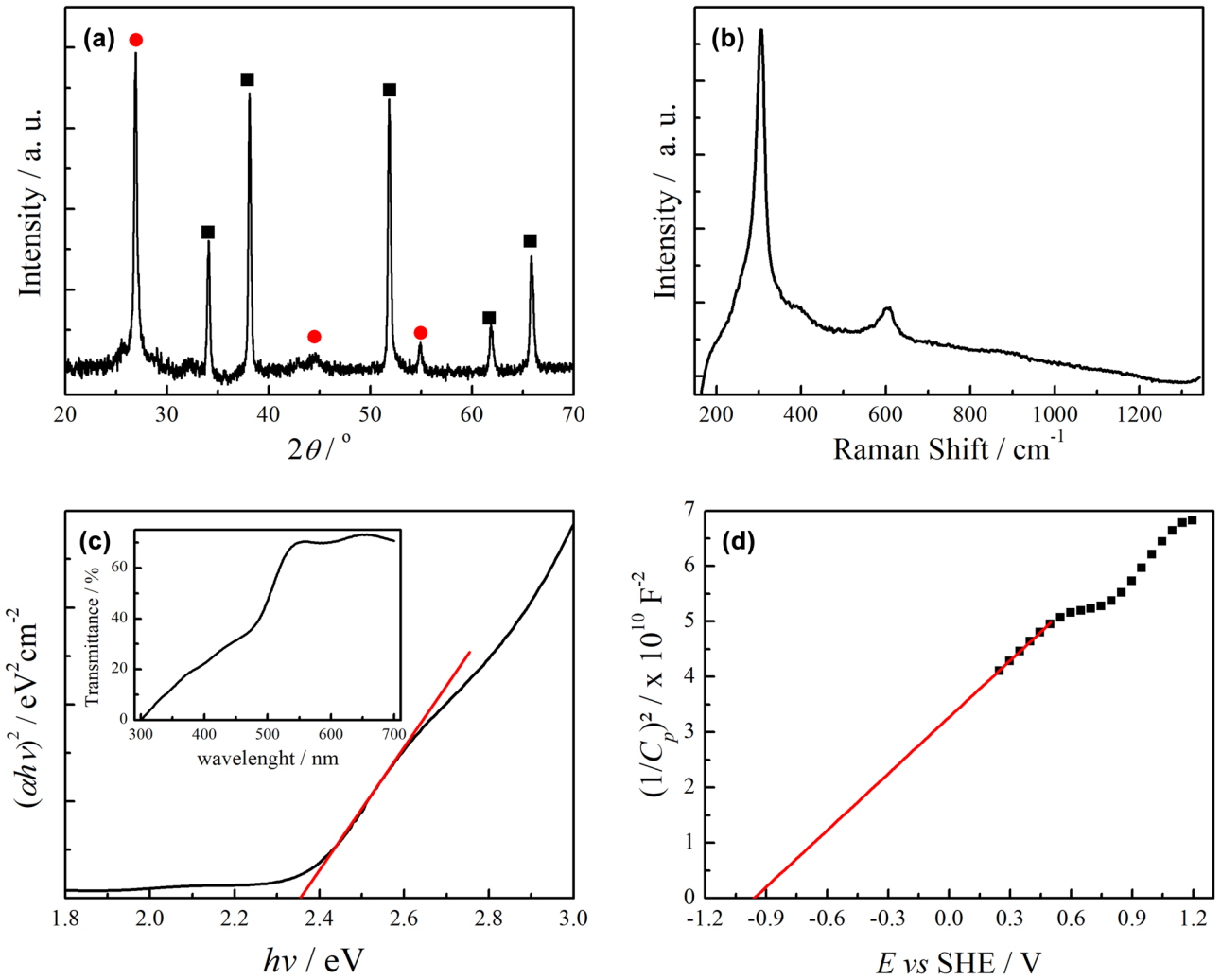

Fig. 1 **a** X-ray diffraction patterns ● represent CdS and ■ represent FTO diffraction peaks. **b** Raman spectra. **c** Tauc plot with n = 1/2, inset: UV–Vis spectra. **d** Mott-Schottky plot

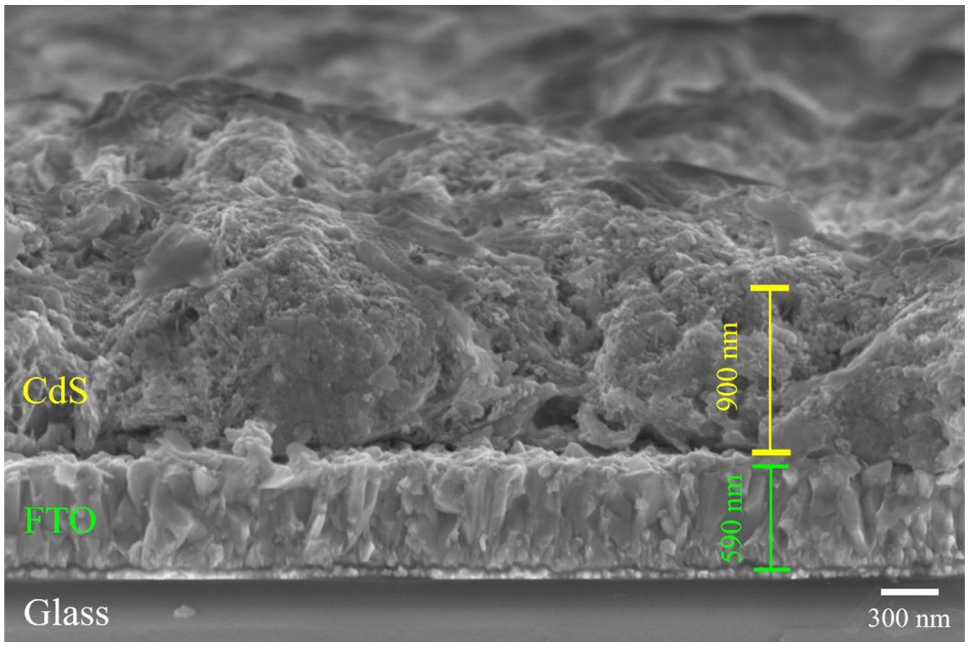

Fig. 2 Cross-section SEM image for CdS thin films deposited into FTO

(a) shows the linear potential voltammogram at 5 mV s^{-1} from 0.0 to 1.0 V (*vs* RHE) in the dark (dotted lines) and simulated solar light (continuous lines) and the plate (b) the same experiment but in intermittent light conditions i.e., on/off regime. Finally, the plate (c) brings the currents observed in the presence of light along 1 h with constant potential of 0.6 V (chronoamperometry experiment). Regardless the method employed, the activity, in terms of photocurrents, follows the order: $j_{sulfite} > j_{glycerol} > j_{water}$.

Glycerol was also replaced by ethylene glycol and methanol to compare the CdS activity for the oxidation of distinct organic molecules. Figure 4(a) and (b) shows the linear potential voltammograms under intermittent solar illumination and the chronoamperograms at 0.6 V for the three organic molecules studied in this work, respectively. The error bar represents the standard deviation along the time-series for the three distinct experiments with three distinct electrodes (prepared with identical conditions) for each organic molecule. The plate (c) brings an overview of the currents registered for all the systems after 1 h at 0.6 V.

The CdS films employed for water, glycerol, methanol, and sulfite chronoamperometry experiments were cut and analyzed after the electrochemical tests. The SEM imagens (cross-sections) of these films are shown in Fig. 5.

Discussion

The obtained XRD analysis (Fig. 1a) has a good match with patterns for cubic CdS and tetragonal SiO_2 from the glass substrate, JCPDS-ICDD Card No. 01-075-0581 and JCPDS-ICDD No. 41-1445, respectively. The CdS diffraction peak located at $2\theta = 26.9°$ corresponds to the (0 0 2) hexagonal plane or the (1 1 1) cubic plane of CdS, the peak at $2\theta = 44.5°$ can be assigned to the (1 1 0) hexagonal plane or (2 2 0) cubic plane [25] and the peak at $2\theta = 54.7°$ assigns to the (3 1 1) plane of the cubic CdS [26]. Thus, the presence of the peak at 54.7° and the absence of the peaks relative to the hexagonal diffraction for the (1 0 0) and (1 0 1) planes [27] indicate the cubic crystal phase was obtained. The two bands observed on the Raman spectra (Fig. 1b) also agree with the CdS film structure. Both XRD and Raman spectra agree with the observed patterns for the cubic phase found in other papers where CdS films were prepared in similar conditions [25, 28].

The as-prepared film absorption band at wavelengths lower than 520 nm (Fig. 1c) is in good agreement with the value for the CdS band gap [29]. The band gap energy (E_g) was obtained by the Tauc plot [30] according to Eq. (8):

$$(\alpha h\nu)^{1/n} = A(h\nu - E_g) \tag{8}$$

where α is the absorption coefficient; $h\nu$ is the energy of the incident photons; n is the transition coefficient; and A is a constant. The Tauc plot revealed a $E_g = 2.36$ eV, in good agreement with CdS thin film in the literature [31]. The coefficient n is dependent on the transition type, and was set as $n = ½$ i.e., a direct allowed transition.

The Mott-Schottky plot (Fig. 1d) was based in the potential region employed for the photoelectrochemical measurements, which was from 0.0 to 1.0 V vs RHE. The positive slope indicates a n-type semiconductor and the interception of linear region with the x-axis ($1/C^2 = 0$) gives a –0.96 V vs SHE flat-band potential value (E_{fb}) in good agreement

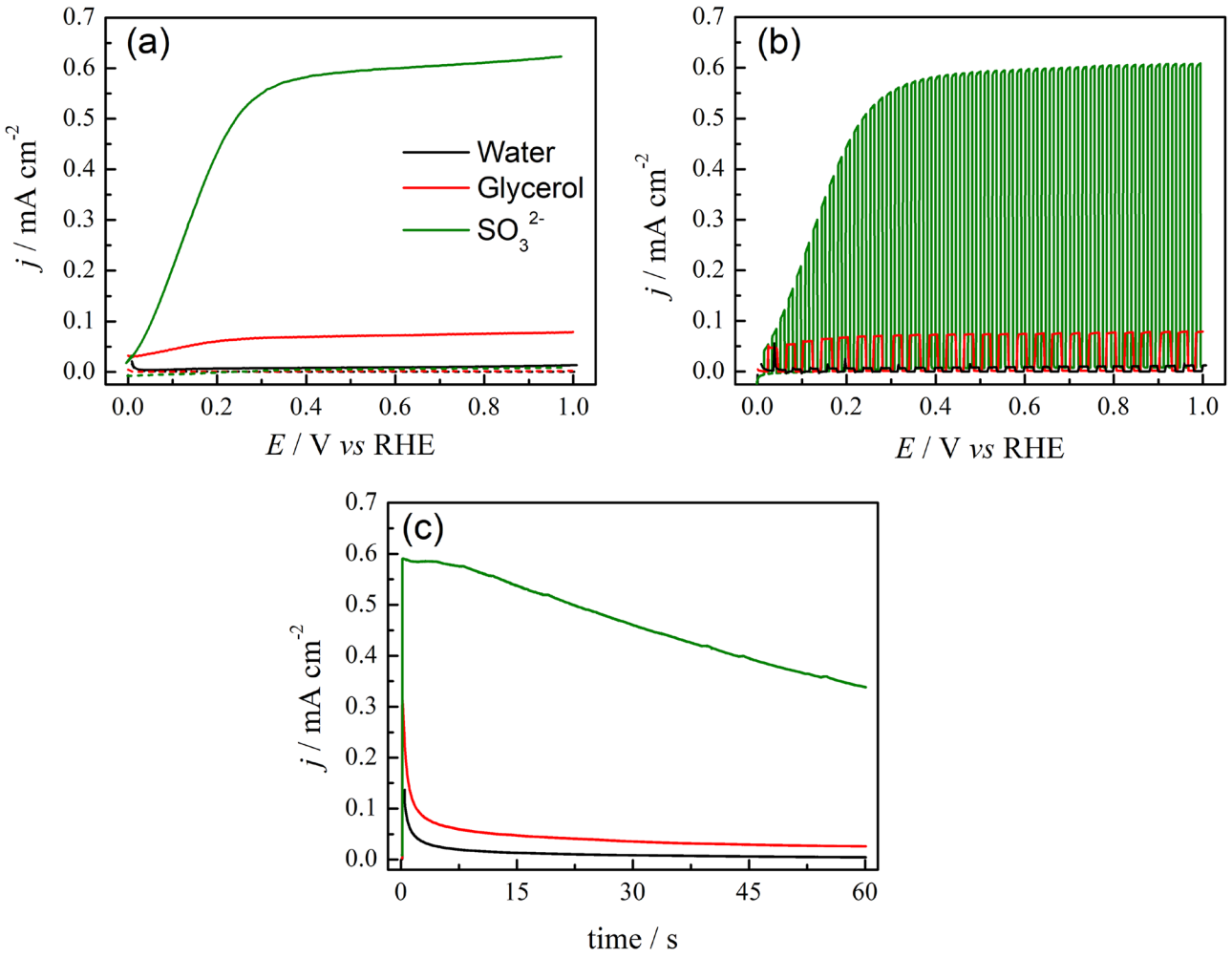

Fig. 3 CdS/FTO photoelectrochemical measurements in a Na_2SO_4 0.5 mol L^{-1} solution for water oxidation (only supporting electrolyte) and after addition of glycerol (1.0 mol L^{-1}) or sulfite anions (1.0 mol L^{-1}). **a** Linear potential voltammograms at 5 mV s^{-1} in the presence (solid) or absence (dotted) simulated solar illumination; **b** linear potential voltammograms under intermittent solar illumination; and **c** chronoamperometry under simulated solar illumination at 0.6 V vs RHE

with the literature [32]. The E_{fb} is related with the conduction band (CB) for a n-type semiconductor and, taking the bang gap value obtained from Tauc plot into account, it is possible to determine the valence band (VB) energy as 1.40 V vs SHE. The Mott-Schottky plot slope also allowed us to estimate the number of charge majority carriers [33] as 4.65×10^{18} electrons and the same value for holes, once the CdS is an intrinsic semiconductor, i.e. once it has no impurities, the number of its charge carriers is determined by the material properties itself and the number of electrons and holes are the same.

The globular structure of the film agrees with the literature of CdS chemical bath deposition [34], as also the structural, optical, and microscopy characterizations of the CdS films, which confirms the synthesis of CdS film deposited into FTO substrates.

The energy values estimated for conduction band (CB), valence band (VB), and band gap (*E*g) were used to build the scheme shown in Fig. 6.

The electrochemical experiments showed photocurrents for water oxidation reaction in all potential region of the linear potential voltammogram in Fig. 3b (higher currents in the presence of simulated light than in the dark conditions); however, these photocurrents do not exceed more than 10 µAcm^{-2}. Glycerol is a better hole scavenger than water, as can be observed by the photocurrents increase in the region from 0.0 to 0.2 V vs RHE and are quite stable from 0.2 to 1.0 V vs RHE reaching ca 70 µAcm^{-2}. Likewise, ethylene glycol has higher photocurrent values than water and methanol in the region from 0.0 to1.0 V vs RHE. When compared to glycerol its values are similar in the higher potential region (Fig. 4a). Despite the three of them being

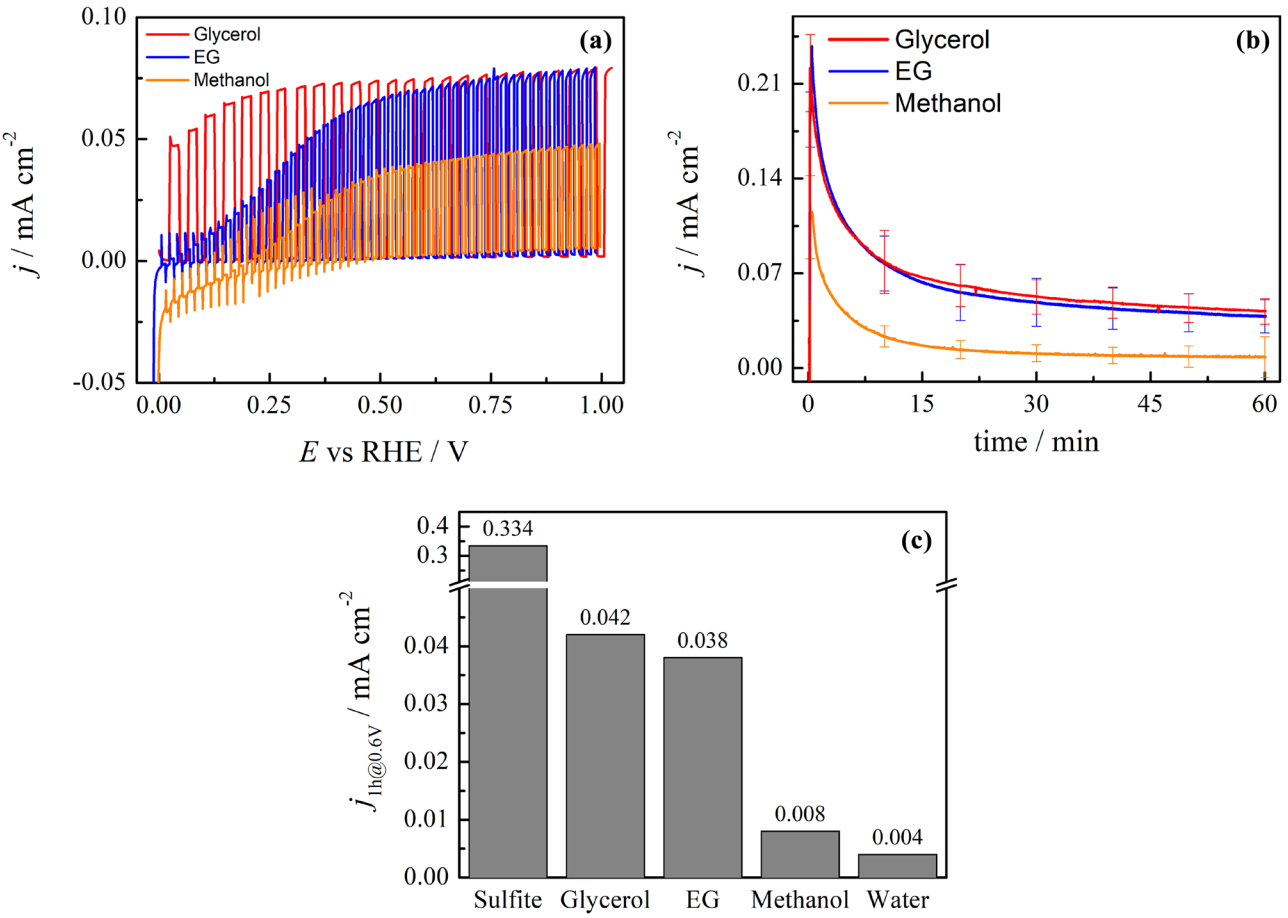

Fig. 4 CdS/FTO photoelectrochemical measurements in a Na_2SO_4 0.5 mol L^{-1} solution for water oxidation (only supporting electrolyte) and after addition of glycerol, ethylene glycol, or methanol in sufficient amount to yield 1.0 mol L^{-1}. **a** Linear potential voltammograms at 5 mV s^{-1} under intermittent simulated solar illumination and **b** chronoamperometry under continuous simulated solar illumination at 0.6 V vs RHE. **c** Each studied molecule currents registered under simulated solar illumination at 0.6 V vs RHE after 1 h

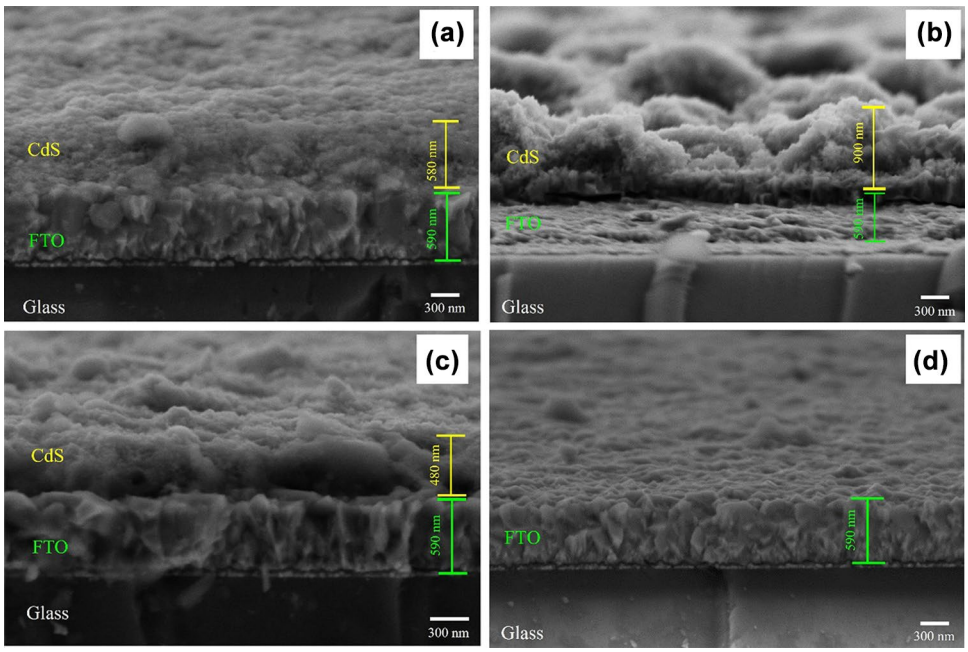

Fig. 5 Cross-section SEM images for CdS thin films deposited on FTO after chronoamperometric experiment for 1 h at 0.6 V vs ERH in Na_2SO_4 0.5 mol L^{-1} under sunlight-simulated illumination. with addition of **a** Na_2SO_3 0.5 mol L^{-1}; **b** glycerol 1.0 mol L^{-1}; **c** methanol 1.0 mol L^{-1}; and **d** only in supporting electrolyte

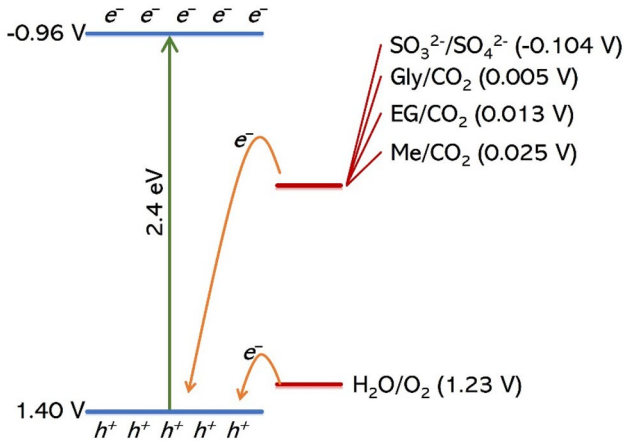

Fig. 6 Band energy scheme based on the energy values measured for synthetized CdS film. Me = methanol, EG = ethylene glycol, and Gly = glycerol

small alcohols, methanol has a lower activity than ethylene glycol and glycerol in all the potential range studied. Sulfite oxidation provides photocurrents up to 0.6 mAcm^{-2} indicating that while the photocurrents for organic molecules are higher than that observed to OER, the photogenerated holes are not completely consumed.

About the sulfite oxidation, it is important highlight that at pH 6.5, both SO_3^{2-} and HSO_3^- (hydrogen sulfite anion) exists in solution. The sulfite oxidation to sulfate (Eq. 13) involves only two electrons and has a lower standard potential than water (Eq. 9). The sulfite oxidation can also yield $S_2O_6^{2-}$ or $SO_3^{\bullet-}$ (radical); however, these species can be further oxidized yielding sulfate as product. Herein, it is important to mention that the direct dissolution of Na_2SO_3 into unbuffered solution such as Na_2SO_4 raises the pH; for instance, the addition of Na_2SO_3 in sufficient amount to yields 1.0 mol L^{-1} modified the pH from 6.5 to 9.0. Figure 7 shows the linear potential voltammograms under intermittent

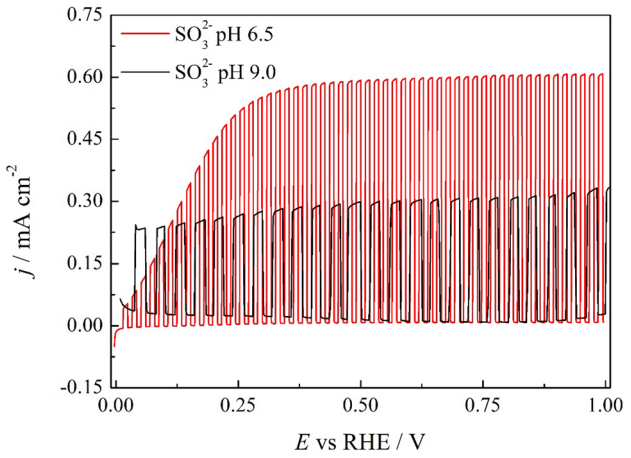

Fig. 7 Linear potential voltammogram under intermittent solar irradiation using CdS/FTO photoanode in a Na_2SO_4 0.5 mol L^{-1} supporting electrolyte after addition of Na_2SO_3 1.0 mol L^{-1}

solar irradiation using the CdS/FTO photoanode in Na_2SO_4 0.5 mol L^{-1} solution after addition of Na_2SO_3 (mol L^{-1}) with pH correction to 6.5 (red) and without pH correction (black line). Clearly, higher photocurrents are obtained in pH 6.5 than in pH 9.0, highlighting the importance of maintain the same experimental condition to compare distinct analytes.

Based on thermodynamic data, all the reactions studied can donate electrons to CdS holes (h^+), as inferred by the standard potentials (E^0/vs SHE) to alcohol/CO_2 and sulfite/sulfate equilibriums (Eqs. 9–13). These potentials were used to build the scheme shown in Fig. 6.

$$O_2 + 4H^+ + 4e^- \rightleftharpoons 2H_2O \; E^0 = 1.229 \tag{9}$$

$$CO_2 + 6H^+ + 6e^- \rightleftharpoons CH_3OH + H_2O \; E^0 = 0.025 \tag{10}$$

$$2CO_2 + 10H^+ + 10e^- \rightleftharpoons (CH_2OH)_2 + 2H_2O \; E^0 = 0.013 \tag{11}$$

$$3CO_2 + 14H^+ + 14e^= \rightleftharpoons C_3H_8O_3 + 3H_2O \; E^0 = 0.005 \tag{12}$$

$$SO_4^{2-} + 2H^+ + 2e^- \rightleftharpoons SO_3^{2-} + H_2O \; E^0 = -0.104 \tag{13}$$

Sulfite can capture the holes with the best efficiency when compared to the other species, even with chemical equilibrium converting part of sulfite to hydrogen sulfite as above mentioned. Although the alcohols do not set a chemical equilibrium in aqueous solution, the methanol, ethylene glycol, and glycerol oxidation mechanisms are more complex than sulfite, especially by the possibility to exchange a large number of electrons per molecule, for example, glycerol oxidation can start by losing 2e$^-$, yielding aldehyde or ketone, or going to higher oxidation states loosing up to 14e$^-$ to yield CO_2. It is also important to considerer that organic molecules can adsorb on the semiconductor which prevent new molecules to arrive on the photoanode surface, lowering the conversion efficiency.

Although one could relate the standard potentials to alcohol/CO_2 equilibriums with the photocurrents values, these potentials are very close for methanol, ethylene glycol, and glycerol when compared to the water oxidation; however, considering the photocurrent after 1 h at 0.6 V for water oxidation, this value is increased by two and ten times in the presence of methanol and glycerol/ ethylene glycol, respectively which allow us to conclude that the reactivity is not straightforwardly related to the standard potential even for species with similar function groups. Moreover, the methanol oxidation to partially oxidized products such as formaldehyde (Eq. 14) or formic acid (Eq. 15) also depict standard potentials [35] that allow the spontaneous reaction with h^+.

$$CH_2O + 2H^+ + 2e^- \rightleftharpoons CH_3OH \; E^0 = 0.319 \tag{14}$$

$$HCOOH + 4H^+ + 4e^- \rightleftharpoons CH_3OH + H_2O \; E^0 = 0.161 \quad (15)$$

Conventionally sacrificial agents containing hydroxyl groups are essential to efficient H_2 evolution in photoelectrochemical cells (PEC) [36, 37]. However, it is still not clear if the increase in the structure complexity can enhance the system performance. Some works show that increasing sacrificial agent complexity decreases the H_2 production rates [38, 39], while other ones show the opposite effect [40, 41]. This contradiction may be explained by the electronic and physical characteristics of the semiconductor catalysts that rules the photoactivity, as well as other factors such as the nature of the electrolyte, local pH, temperature, sacrificial agent concentration, and its interaction with the catalyst surface. Fu et al. reported that in a Pt/TiO_2 photocatalyst, higher H_2 and CO_2 evolution were observed when the number of hydroxyl groups was increased in the molecules in the order: isopropanol < propylene glycol < glycerol [41], these findings could be attributed to a dual characteristic of the hydroxyl groups: effective h^+ scavengers and good anchors for adsorption on TiO_2, as observed here for CdS.

We have mapped the products of electrochemical glycerol photooxidation by hematite observing a low selectivity and near zero activation energy [42]. The results were interpreted as mechanism involving an adsorbed or near to surface radical that will provides distinct products depending on the formation of the hole on the surface. In the present work, the polyalcohol molecules have higher activity because their hydroxyl groups are more susceptible to interact with the CdS surface, once it has two or more hydroxyl groups. Contrary, methanol has only one hydroxyl group, which makes weaker interactions with the CdS.

Finally, the CdS is not stable in pH below 8. The oxidation process in aqueous media consumes OH^- (see Eq. 5) or releases H^+ leading to the pH decrease and contribute to the stabilization of the cation Cd^{2+} in solution [43], and the consumption of S^{2-} as shown in Eq. 6, which highlights the CdS dissolution. This, in fact, is enhanced when the CdS is directly illuminated, because regardless the presence of oxygen, the photogenerated holes oxidize CdS which contribute to the film corrosion (Eqs. 1–3).

The morphological analysis of the films after the electrochemical aging tests (Fig. 5) clearly shows that the decreasing in thickness depends on the hole scavenger in the electrolyte. The OER (Fig. 5d) was the reaction that almost completely vanished the film due to the photocorrosion reaction. In the case of sulfide oxidation reaction, the film thickness decreases almost a half, but keeping its globular packed morphology as shown in the image of pristine film (Fig. 2).

Interesting, despite the decrease of pH due to the oxidation processes increase the CdS chemical degradation, the presence of alcohols on the solution seems to prevent the CdS film corrosion. The CdS film thickness after the glycerol experiment seems to keep as high as the initial pristine thickness (see Figs. 5b and 2). This can be interesting, because even though glycerol does not present the same photocurrent as sulfite, it can remain stable for longer periods, being more efficient in long-term analysis than sulfite which suffers a loss of 50% of the initial thickness value of the film. In the presence of alcohol, the morphology seems to be changed and a floccular structure grows over the compact globular CdS. The mechanism of the morphological/structural changes is under investigation.

Conclusion

In this work, we reported the fabrication of CdS photoanode films with a globular morphology by a chemical method deposition, which is easily photocorroded due to the reaction between the photogenerated holes on the valence band of the semiconductor material and the sulfur anions, as part of the film composition. A strong relationship between the photocurrent and the presence of a hole scavenge present in the electrolyte was found for all investigated small organic molecules, which shows the reactivity depends on the number of aliphatic alcohols groups presented in the molecule: methanol, ethylene glycol, and glycerol. Based on these results, we can expect promoting the small organic molecules oxidation, in particular, glycerol, over the photocorrosion reaction on CdS surface, on the basis of the linear potential voltammetry and chronoamperometric experiments under simulated sunlight conditions. Glycerol oxidation was found as an ideal hole scavenger having the compromise to get the photogenerated roles on CdS valence band and decreases the film dissolution in comparison with other organic and inorganic compounds. Finally, although the photocurrents observed for organic molecules are lower than those observed for SO_3^{2-} oxidation, the organic molecules open the possibility to produce added-value compounds on PEC anodes concomitant to H_2 production on the cathode.

Acknowledgements The authors gratefully acknowledge the support from the FAPESP (Sao Paulo Research Foundation): (grants: #2013/07296-2 and 2017/11986-5), Brazilian Council for Scientific and Technological Development (CNPq) (Grant # 402481/2021-6) and Shell and the strategic importance of the support given by the ANP (Brazilian National Oil, Natural Gas and Biofuels Agency) through the R&D levy regulation.

Funding This study was financed in part by the Coordenação de Aperfeiçoamento de Pessoal de Nível Superior – Brasil (CAPES) – Pessoal de Nível SuperiorFinance Code 001.

References

1. Jing D, Guo L (2007) Efficient hydrogen production by a composite CdS/mesoporous zirconium titanium phosphate photocatalyst

under visible light. J Phys Chem C 111:13437–13441. https://doi.org/10.1021/jp071700u
2. Wu K, Chen Z, Lv H, Zhu H, Hill CL, Lian T (2014) Hole removal rate limits photodriven H_2 generation efficiency in CdS-Pt and CdSe/CdS-Pt semiconductor nanorod-metal tip heterostructures. J Am Chem Soc 136:7708–7716. https://doi.org/10.1021/ja5023893
3. Simon T, Bouchonville N, Berr MJ, Vaneski A, Adrovic A, Volbers D, Wyrwich R, Döblinger M, Susha AS, Rogach AL, Jäckel F, Stolarczyk JK, Feldmann J (2014) Redox shuttle mechanism enhances photocatalytic H_2 generation on ni-decorated CdS nanorods. Nat Mater 13:1013–1018. https://doi.org/10.1038/NMAT4049
4. Wang C, Wang L, Jin J, Liu J, Li Y, Wu M, Chen L, Wang B, Yang X, Su BL (2016) Probing effective photocorrosion inhibition and highly improved photocatalytic hydrogen production on monodisperse PANI@CdS core-shell nanospheres. Appl Catal B 188:351–359. https://doi.org/10.1016/j.apcatb.2016.02.017
5. Weng B, Qi M-Y, Han C, Tang Z-R, Xu Y-J (2019) Photocorrosion inhibition of semiconductor-based photocatalysts: basic principle, current development and future perspective. ACS Catal 9:4642–4687. https://doi.org/10.1021/acscatal.9b00313
6. Meissner D, Memming R, Shuben L, Yesodharan S, Griitzel M (1985) Photocorrosion by oxygen uptake in aqueous cadmium sulphide suspensions. Ber Bunsenges Phys Chem 89:121–124. https://doi.org/10.1002/bbpc.19850890208
7. Henglein A (1982) Photo-degradation and fluorescence of colloidal-cadmium sulfide in aqueous solution. Ber Bunsenges Phys Chem 86:301–305. https://doi.org/10.1002/bbpc.19820860409
8. Wang R, Wang L, Zhou Y, Zou Z (2019) Al-ZnO/CdS photoanode modified with a triple functions conformal TiO_2 film for enhanced photoelectrochemical efficiency and stability. Appl Catal B 255:117738. https://doi.org/10.1016/j.apcatb.2019.05.040
9. Ouyang J, Chang M, Li X (2012) CdS-sensitized ZnO nanorod arrays coated with TiO_2 layer for visible light photoelectrocatalysis. J Mater Sci 47:4187–4193. https://doi.org/10.1007/s10853-012-6273-x
10. Ho TA, Bae C, Joe J, Yang H, Kim S, Park JH, Shin H (2019) Heterojunction photoanode of atomic-layer-deposited MoS_2 on single-crystalline CdS nanorod arrays. ACS Appl Mater Interfaces 11:37586–37594. https://doi.org/10.1021/acsami.9b11178
11. Li X, Zhang Z, Chen L, Liu Z, Cheng J, Ni W, Xie E, Wang B (2014) Cadmium sulfide quantum dots sensitized tin dioxide-titanium dioxide heterojunction for efficient photoelectrochemical hydrogen production. J Power Sources 269:866–872. https://doi.org/10.1016/j.jpowsour.2014.07.060
12. Weng B, Liu S, Zhang N, Tang ZR, Xu YJ (2014) A simple yet efficient visible-light-driven CdS nanowires-carbon nanotube 1D–1D nanocomposite photocatalyst. J Catal 309:146–155. https://doi.org/10.1016/j.jcat.2013.09.013
13. Berr MJ, Wagner P, Fischbach S, Vaneski A, Schneider J, Susha AS, Rogach AL, Jäckel F, Feldmann J (2012) Hole scavenger redox potentials determine quantum efficiency and stability of Pt-decorated CdS nanorods for photocatalytic hydrogen generation. Appl Phys Lett 100:223903. https://doi.org/10.1063/1.4723575
14. Bao N, Shen L, Takata T, Domen K (2008) Self-templated synthesis of nanoporous CdS nanostructures for highly efficient photocatalytic hydrogen production under visible light. Chem Mat 20:110–117. https://doi.org/10.1021/cm7029344
15. Waterston K, Bejan D, Bunce NJ (2007) Electrochemical oxidation of sulfide ion at a boron-doped diamond anode. J Appl Electrochem 37:367–373. https://doi.org/10.1007/s10800-006-9267-z
16. Lu X, Xie S, Yang H, Tong Y, Ji H (2014) Photoelectrochemical hydrogen production from biomass derivatives and water. Chem Soc Rev 43:7581–7593. https://doi.org/10.1039/c3cs60392j
17. Mesa CA, Kafizas A, Francàs L, Pendlebury SR, Pastor E, Ma Y, le Formal F, Mayer MT, Grätzel M, Durrant JR (2017) Kinetics of photoelectrochemical oxidation of methanol on hematite photoanodes. J Am Chem Soc 139:11537–11543. https://doi.org/10.1021/jacs.7b05184
18. Che Mat AN, Sairi NA, Basirun WJ, Rezayi M, Mat Teridi MA, Mazhar M (2019) Photoelectrocatalytic oxidation of methanol over RuO_2–MnO_2–Co_3O_4 supported porous anatase under visible light irradiation. Mater Chem Phys 224:196–205. https://doi.org/10.1016/j.matchemphys.2018.12.018
19. Kang S, Xia F, Zhuofeng Hu, Hu W, She Y, Wang L, Fu X, Lu W (2020) Platinum nanoparticles with TiO_2–skin as a durable catalyst for photoelectrochemical methanol oxidation and electrochemical oxygen reduction reactions. Electrochim Acta 343:136119. https://doi.org/10.1016/j.electacta.2020.136119
20. Cai Q, Hong W, Li J, Jian C, Liu W (2017) A silicon photoanode for efficient ethanol oxidation under alkaline conditions. RSC Adv 7:21809–21814. https://doi.org/10.1039/c7ra02848b
21. Mascaro LH, Pockett A, Mitchels JM, Peter LM, Cameron PJ, Celorrio V, Fermin DJ, Sagu JS, Wijayantha KGU, Kociok-Köhn G, Marken F (2015) One-step preparation of the $BiVO_4$ film photoelectrode. J Solid State Electrochem 19:31–35. https://doi.org/10.1007/s10008-014-2495-y
22. Byrne JA, Eggins BR (1998) Photoelectrochemistry of oxalate on particulate TiO_2 electrodes. J Electroanal Chem 457:61–72. https://doi.org/10.1016/S0022-0728(98)00304-0
23. Kwon Y, Schouten KJP, Koper MTM (2011) Mechanism of the catalytic oxidation of glycerol on polycrystalline gold and platinum electrodes. ChemCatChem 3:1176–1185. https://doi.org/10.1002/cctc.201100023
24. Liu D, Liu JC, Cai W, Ma J, Yang H, bin, Xiao H, Li J, Xiong Y, Huang Y, Liu B, (2019) Selective photoelectrochemical oxidation of glycerol to high value-added dihydroxyacetone. Nat Commun 10:1779. https://doi.org/10.1038/s41467-019-09788-5
25. Liu F, Lai Y, Liu J, Wang B, Kuang S, Zhang Z, Li J, Liu Y (2010) Characterization of chemical bath deposited CdS thin films at different deposition temperature. J Alloys Compd 493:305–308. https://doi.org/10.1016/j.jallcom.2009.12.088
26. Zyoud A, Saa'Deddin I, Khudruj S, Hawash ZM, Park D, Campet G, Hilal HS, (2013) CdS/FTO thin film electrodes deposited by chemical bath deposition and by electrochemical deposition: a comparative assessment of photo-electrochemical characteristics. Solid State Sci 18:83–90. https://doi.org/10.1016/j.solidstatesciences.2013.01.004
27. Mahdi MA, Hassan Z, Ng SS, Hassan JJ, Bakhori SKM (2012) Structural and optical properties of nanocrystalline CdS thin films prepared using microwave-assisted chemical bath deposition. Thin Solid Films 520:3477–3484. https://doi.org/10.1016/j.tsf.2011.12.059
28. Trajić J, Gilić M, Romčević N, Romčević M, Stanišić G, Hadžić B, Petrović M, Yahia YS (2015) Raman spectroscopy of optical properties in CdS thin films. Sci Sinter 47:145–152. https://doi.org/10.2298/SOS1502145T
29. Choi JY, Kim K-J, Yoo J-B, Kim D (1998) Properties of cadmium sulfide thin films deposited by chemical bath deposition with ultrassonication. Sol Energy 64:41–47. https://doi.org/10.1016/S0038-092X(98)00047-4
30. Escobedo-Morales A, Ruiz-L opez II, Ruiz-Peralta M, Tepech-Carrillo L, anchez-Cant MS, Moreno-Orea JE, (2019) Automated method for the determination of the band gap energy of pure and mixed powder samples using diffuse reflectance spectroscopy. Heliyon 5:e01505. https://doi.org/10.1016/j.heliyon.2019
31. Shan Y, Zhao J, Li W, Huang Q, Xiao C (2018) Dual effect of polypyrrole doping on cadmium sulfide for enhanced photocatalytic activity and robust photostability. J Mater Sci 53:2065–2076. https://doi.org/10.1007/s10853-017-1630-4
32. Weng YC, Chang H (2016) Screening and characterization for the optimization of CdS-based photocatalysts. RSC Adv 6:41376–41384. https://doi.org/10.1039/c6ra05245b

33. Nasir SNS, Mohamed NA, Tukimon MA, Noh MFM, Arzaee NA, Teridi MAM (2021) Direct extrapolation techniques on the energy band diagram of $BiVO_4$ thin films. Physica B Condens Matter 604:412719. https://doi.org/10.1016/j.physb.2020.412719
34. Rafiq A, Imran M, Aqeel M, Naz M, Ikram M, Ali S (2020) Study of transition metal ion doped CdS nanoparticles for removal of dye from textile wastewater. J Inorg Organomet Polym Mater 30:1915–1923. https://doi.org/10.1007/s10904-019-01343-5
35. Vielstich W (1970) Fuel cells: modern processes for the electrochemical production of energy. Wiley-Interscience, New York
36. Tran H, Chiang K, Scott J, Amal R (2005) Understanding selective enhancement by silver during photocatalytic oxidation. Photochem Photobiol Sci 4:565–567. https://doi.org/10.1039/b506320e
37. Bowker M, Davies PR, Al-Mazroai LS (2009) Photocatalytic reforming of glycerol over gold and palladium as an alternative fuel source. Catal Letters 128:253–255. https://doi.org/10.1007/s10562-008-9781-1
38. Carraro G, MacCato C, Gasparotto A, Montini T, Turner S, Lebedev OI, Gombac V, Adami G, van Tendeloo G, Barreca D, Fornasiero P (2014) Enhanced hydrogen production by photoreforming of renewable oxygenates through nanostructured Fe_2O_3 polymorphs. Adv Funct Mater 24:372–378. https://doi.org/10.1002/adfm.201302043
39. Rodriguez J, Thivel PX, Puzenat E (2013) Photocatalytic hydrogen production for PEMFC supply: a new issue. Int J Hydrogen Energy 38:6344–6348. https://doi.org/10.1016/j.ijhydene.2013.03.026
40. Strataki N, Bekiari V, Kondarides DI, Lianos P (2007) Hydrogen production by photocatalytic alcohol reforming employing highly efficient nanocrystalline titania films. Appl Catal B 77:184–189. https://doi.org/10.1016/j.apcatb.2007.07.015
41. Gu Q, Fu X, Wang X, Chen S, Leung DYC, Xie X (2011) Photocatalytic reforming of C3-polyols for H_2 production. Part II. FTIR study on the adsorption and photocatalytic reforming reaction of 2-propanol on Pt/TiO_2. Appl Catal B 106:689–696. https://doi.org/10.1016/j.apcatb.2011.05.046
42. Perini N, Hessel C, Bott-Neto JL, Pires CTGVMT, Fernandez PS, Sitta E (2021) Photoelectrochemical oxidation of glycerol on hematite: thermal effects, in situ FTIR and long-term HPLC product analysis. J Solid State Electrochem 25:1101–1110. https://doi.org/10.1007/s10008-020-04878-7
43. Brookins DG (1986) Geochemical behavior of antimony, arsenic, cadmium and thallium: Eh-pH diagrams for 25 °C, 1-bar pressure. Chem Geol 54:271–278. https://doi.org/10.1016/0009-2541(86)90141-5